

FALO: Fast and Accurate LiDAR 3D Object Detection on Resource-Constrained Devices

Shizhong Han¹ Hsin-Pai Cheng¹ Hong Cai¹ Jihad Masri² Soyeb Nagori² Fatih Porikli¹

¹Qualcomm AI Research* ²Qualcomm Technologies, Inc.

{shizhan, hsinpaic, hongcai, jmasri, soyeb, fporikli}@qti.qualcomm.com

Abstract

Existing LiDAR 3D object detection methods predominantly rely on sparse convolutions and/or transformers, which can be challenging to run on resource-constrained edge devices, due to irregular memory access patterns and high computational costs. In this paper, we propose FALO, a hardware-friendly approach to LiDAR 3D detection, which offers both state-of-the-art (SOTA) detection accuracy and fast inference speed. More specifically, given the 3D point cloud and after voxelization, FALO first arranges sparse 3D voxels into a 1D sequence based on their coordinates and proximity. The sequence is then processed by our proposed ConvDotMix blocks, consisting of large-kernel convolutions, Hadamard products, and linear layers. ConvDotMix provides sufficient mixing capability in both spatial and embedding dimensions, and introduces higher-order nonlinear interaction among spatial features. Furthermore, when going through the ConvDotMix layers, we introduce implicit grouping, which balances the tensor dimensions for more efficient inference and takes into account the growing receptive field. All these operations are friendly to run on resource-constrained platforms and FALO can readily deploy on compact, embedded devices. Our extensive evaluation on LiDAR 3D detection benchmarks such as nuScenes and Waymo shows that FALO achieves competitive performance. Meanwhile, FALO is 1.6~9.8 \times faster than the latest SOTA on NVIDIA Graphics Processing Unit (GPU) and Qualcomm Neural Processing Unit (NPU).¹

1. Introduction

Perceiving objects based on 3D LiDAR point cloud is critical to various applications, such as autonomous driving, robotics, and AR/VR. Unlike cameras, LiDAR sensors directly measure distances, and are robust to varying illumi-

¹Snapdragon and Qualcomm branded products are products of Qualcomm Technologies, Inc. and/or its subsidiaries. Qualcomm patented technologies are licensed by Qualcomm Incorporated.

*Qualcomm AI Research is initiative of Qualcomm Technologies, Inc.

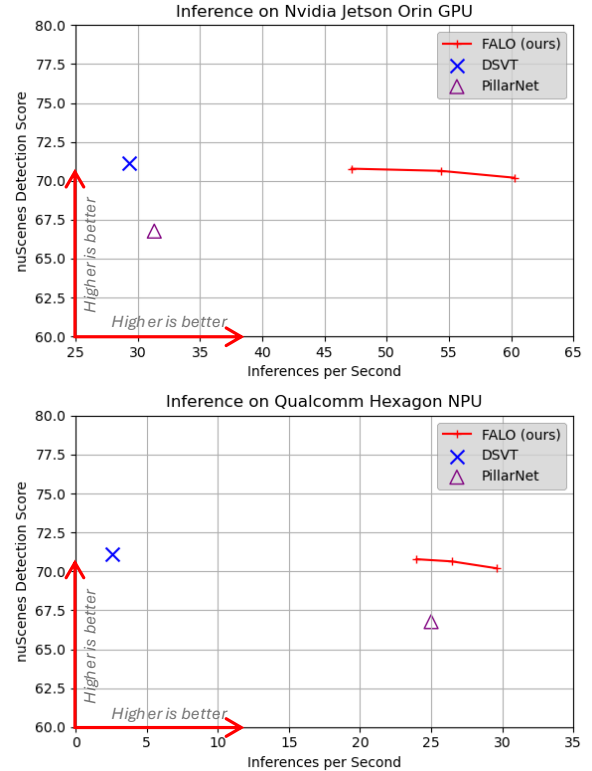


Figure 1. Comparison of 3D object detection accuracy (nuScenes Detection Score on nuScenes validation) vs. inference speed (inferences per second) on two embedded platforms: Nvidia Jetson Orin GPU (left) and Qualcomm® Hexagon™ NPU which is integrated within the Snapdragon® 8 Gen 3 processor (right). For feasible deployment on device, we select models that do not use sparse convolutions. Specifically, DSVT [40] is the only latest SOTA method that does not use sparse convolutions. Additionally, we use a modified version of PillarNet [33], which replaces sparse convolutions with dense ones and has similar accuracy as the original model.

nation and weather conditions, providing more reliability and safety to the autonomous system. Moreover, in recent years, LiDAR sensors have become more affordable, making it more economical to use them in production systems.

Existing methods for LiDAR-based 3D object detection

predominantly utilize 3D sparse convolutions to process the 3D voxels [9, 11, 15, 22, 35, 39, 42, 47, 49, 55]. While sparse convolution is more computationally and memory efficient compared to regular dense convolution, it incurs irregular data and memory access patterns due to the inherent sparsity of the 3D point cloud. This poses a challenge for compact, memory-constrained embedded devices. Furthermore, the use of sparse convolutions complicates quantization and deployment of the model via TensorRT [54].

Another line of work leverages pillar-based representation to project 3D voxels to a 2D plane [19]. This significantly improves the computation efficiency thanks to the reduced number of voxels. However, their detection accuracy lags behind models that directly process 3D voxels, and most recent works still require 2D sparse convolutions [21, 33].

More recently, researchers have started to explore transformers for LiDAR 3D object detection [24, 40]. For instance, in DSVT [40], the 3D voxels are treated as tokens and divided into small groups, with self-attention performed within each group. By doing this, DSVT achieves state-of-the-art performance, without using any sparse convolutions. However, transformers incur high computational and memory costs, both of which are quadratic w.r.t. the number of input tokens, *i.e.*, non-empty voxels in this case. A few recent works [25, 50] propose to replace transformers with Recurrent Neural Networks (RNNs) or State-Space Models (SSMs). Since these models are originally designed for auto-regressive tasks, they need to process the voxel tokens sequentially, which is inefficient. Furthermore, they still require sparse convolutions.

In this paper, we propose a fast and accurate approach to LiDAR 3D object detection, FALO, which not only runs on embedded computation units with low latencies but also maintains competitive detection accuracy. Figure 1 shows detection accuracy vs. inference speed comparisons between FALO and the latest state of the art (SOTA), where the inference speeds are measured on Nvidia Jetson Orin GPU and Hexagon NPU (included in the Snapdragon 8 Gen 3 processor), respectively, which are common choices of computation platform for autonomous systems. Note that except for DSVT [40], existing SOTA models cannot even be deployed due to the use of sparse convolutions. Figure 1 demonstrates that the proposed FALO has the highest inference speed on resource-constrained computation platforms while keeping comparable detection accuracy compared with SOTA methods.

At the core of FALO is an efficient, systematic design for processing voxels. More specifically, we first arrange the 3D voxels into a 1D sequence, based on their coordinates and proximity. Next, we utilize large-kernel convolutions and linear layers to perform spatial and channel feature mixing, respectively. In addition, we leverage Hadamard prod-

uct to create higher-order nonlinear interactions among the voxel features. As shown in recent studies on efficient image backbones, such as Conv2Former [18] and PADRe [20], high-order nonlinear processing is crucial for capable vision networks in lieu of the costly self-attention operations. Note that these operations incur only linear computation and memory costs w.r.t. the number of non-empty voxels. Moreover, we maintain a dense representation throughout the network and do not require sparse convolutions, which facilitates more efficient memory access. We pack this series of operations in a layer, which we refer to as ConvDotMix, and repeat the ConvDotMix layer multiple times to process the voxel features, before converting them to Bird’s Eye View (BEV).

Together with ConvDotMix, we introduce implicit grouping to the 1D sequence that better balances the tensor dimensions. This approach improves inference speed by creating tensors with more balanced dimension sizes. We also use variable, increasing implicit group sizes through the ConvDotMix layers, to allow for voxel interaction in wide spatial ranges as the receptive field grows larger.

In addition to not using sparse convolutions, we eliminate other cumbersome and hardware-unfriendly designs in latest SOTA methods [25, 40], *e.g.*, window shifting. At each inference, we only need to perform 1D serialization of the voxels once, unlike existing work [40, 50]; this significantly reduces costly data movement. Finally, all our operations are amenable to parallelization. In addition to these computational advantages, FALO achieves state-of-the-art detection performance, as we will see in the paper.

Our main contributions are summarized as follows:

- We propose FALO, an efficient, systematic approach for fast and accurate LiDAR 3D object detection on resource-constrained computation platforms.
- More specifically, we propose ConvDotMix operations to process the voxel features, which consists of large-kernel convolutions, linear layers, and Hadamard products. ConvDotMix is computationally efficient, and provides sufficient spatial, channel-wise, and higher-order nonlinear mixing capabilities to process the features.
- We introduce additional efficient designs that make inference faster on hardware, *e.g.*, only performing voxel serialization once, implicit voxel grouping. At the same time, we eliminate deployment-unfriendly and/or costly operations used in existing SOTA, such as sparse convolution, self-attention, window shifting, and re-ordering the voxels.
- FALO achieves real-time inference speed on embedded computation platforms, including the Nvidia Jetson Orin GPU and Qualcomm Hexagon NPU. Extensive experiments on standard LiDAR 3D detection benchmarks of nuScenes and Waymo demonstrate the efficiency and effectiveness of our proposed 3D object detection model.

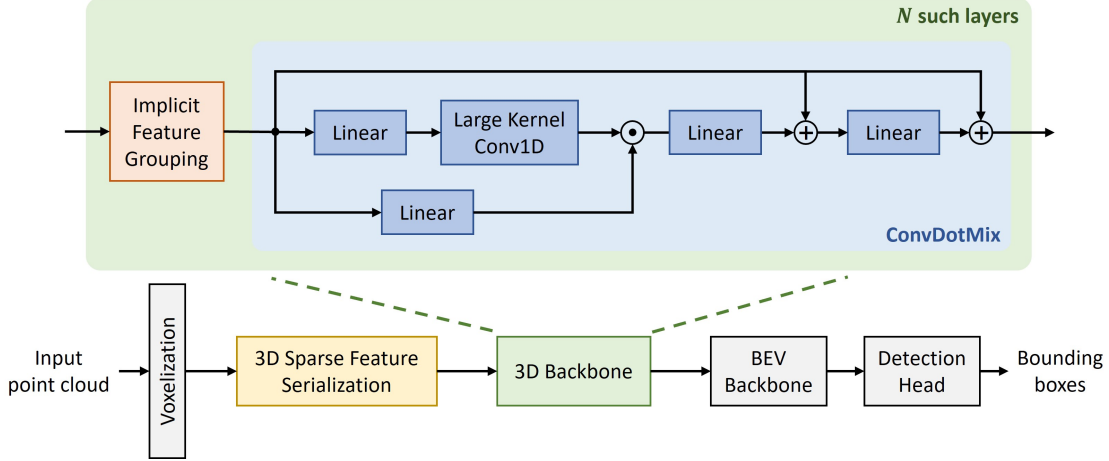


Figure 2. Overview of our proposed FALO approach. Given the input 3D point cloud and after voxelization, we perform 3D sparse feature serialization to arrange the non-empty 3D voxel features into a dense 1D sequence of tokens. The 1D sequence then goes into our 3D backbone, which consists of implicit feature grouping and FALO layers. Implicit grouping reshapes variables from the token dimension to the batch dimension, creating more balanced sizes across the two dimensions. FALO operates on the tokens, mixing them spatially and channel-wise, as well as enabling higher-order nonlinear interaction between the features.

2. Related Work

In 3D perception, two primary methodologies have emerged: **point-based** methods and **voxel-based** methods. Point-based methods [3, 4, 8, 16, 21, 28, 31, 32, 44–46, 52], originating from the PointNet series [29, 30], extract features directly from raw point clouds. Despite their performance in perception tasks, these methods are hindered by the time-consuming processes of point sampling, which incurs irregular memory access, and neighbor searching, which requires expensive computation.

As a result, voxel-based methods [6, 9, 11, 15, 22, 35, 39, 42, 47, 49, 51] have gained prominence in recent years. These methods convert the input point clouds into a structured grid of 3D cells, known as 3D voxels, in which the grids are sparsely occupied. Instead of using the regular, dense 3D convolution, these methods employ 3D sub-manifold sparse convolution, which allows them to significantly reduce memory consumption and computational costs while improving detection accuracy. However, 3D sparse convolution requires customized CUDA operations, involves complex data structures, and incurs irregular memory accesses due to the random sparsity patterns in the data, making it expensive to run on hardware. Specifically, on resource-constrained embedded platforms, where computation capabilities and/or memory bandwidth are limited, it is very challenging, if not infeasible, to run 3D sparse convolutions.

A special case of the voxel-based methods is the **pillar-based** approach, which combines 3D voxels at the same vertical location into a “pillar”. Pillar-based methods are significantly more efficient since there are much fewer grids

to process after projecting the 3D points/voxels onto the bird’s eye view [19, 21, 27, 33, 47, 54]. However, pillar-based methods typically have lower accuracy when compared to voxel-based ones due to their reduced 3D representation capacity, and most of them still require 2D sparse convolutions [21, 33, 47].

Several works have explored **hybrid** approaches, leveraging the strengths of both point-based and voxel-based techniques [34, 36, 43]. For instance, PV-RCNN [34] and its variants [36, 43] integrate point-based and voxel-based features to improve detection accuracy. While these methods aim to balance computational efficiency and feature representation capability, they often face challenges in achieving real-time performance due to the complexity of integrating multiple feature extraction schemes.

More recently, researchers have started to explore processing the voxels in a tokenized way [25, 40, 50]. More specifically, these approaches first serialize the 3D sparse voxels into a 1D dense sequence of tokens, which is then processed using transformers, Recurrent Neural Networks (RNNs), or State-Space Models (SSMs). All of these methods, however, heavily rely on using different orderings of the voxels. For instance, DSVT [40] and LION [25] use alternating x-order and y-order. VoxelMamba [50] requires multi-scale orderings. Re-ordering the voxels several times during inference requires considerable data movement. This incurs expensive memory accesses, especially on compact devices with limited memory bandwidth. Moreover, transformers are computationally expensive with quadratic complexity w.r.t. input size, and latest SSMs, like Mamba [14] require customized CUDA operations, making them infeasible for non-CUDA devices.

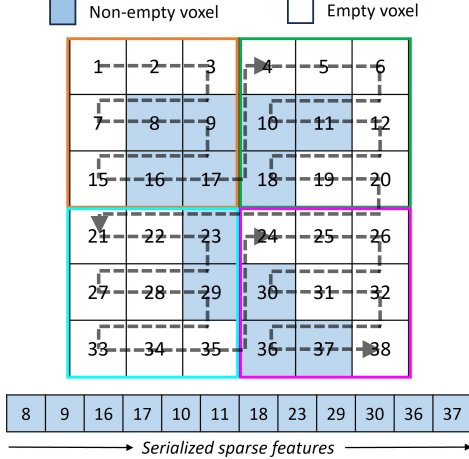


Figure 3. Sparse voxel feature serialization example. The space is divided into local windows (indicated by different colors). The traversal is performed within each window, before proceeding to the next. During this process, the non-empty voxels are collected and arranged into a 1D dense sequence of tokens.

3. Proposed Approach: FALO

In this section, we present our proposed fast and accurate LiDAR 3D object detection approach for edge devices, FALO. We describe our designs that enable FALO, including the serialization of 3D sparse voxels into a dense, 1D sequence of tokens (Section 3.2), hardware-friendly implicit voxel grouping (Section 3.3), and the ConvDotMix operations (Section 3.4).

3.1. System Overview

An overview of our proposed approach is shown in Figure 2. In the LiDAR 3D detection pipeline, the input 3D point cloud is typically first voxelized, *i.e.*, converted into regular 3D grids that are sparsely occupied. This can be done with a voxel feature encoder, such as PointNet [29]. Unlike existing works that directly apply 3D sparse convolution to process the voxel features, we extract the non-empty voxels and arrange them into a dense, 1D sequence of tokens. This facilitates using hardware-friendly, dense operations to process them in our devised 3D backbone, which includes implicit feature grouping and ConvDotMix layers. After the 3D backbone, the voxel features are projected to the Bird’s Eye View (BEV) space and further processed by 2D layers. Finally, a detection head consumes the BEV features and predicts the bounding boxes. We follow standard choices for the BEV backbone and detection head.

3.2. 3D Sparse Feature Serialization

Existing methods use expensive ways to serialize the voxel features, *e.g.*, alternating between x- and y-orders [25, 40], using forward, backward, and multi-scale orders [50]. What

Input Tensor Shape	Latency on NPU (ms)
$1 \times 6000 \times 128$	10.60
$2 \times 3000 \times 128$	9.53
$4 \times 1500 \times 128$	9.00
$10 \times 600 \times 128$	8.40
$20 \times 300 \times 128$	8.12
$60 \times 100 \times 128$	7.99

Table 1. Latencies of inferencing one ConvDotMix layer with different input tensor shapes. The input shape is in batch size \times number of tokens \times embedding dimension. Latency is measured on the Qualcomm Hexagon NPU.

is more, these methods all require re-ordering the voxels multiple times throughout the network layers. This creates costly data movements, especially for devices with limited memory bandwidth.

In FALO, we use an efficient and effective way to arrange the non-empty voxels into a 1D sequence. Figure 3 provides an illustrative example of our approach. First, we divide the voxels into local windows (highlighted with different colors in the figure), and traverse the voxels within each window before proceeding to the next window. In this way, the non-empty voxels in the same local neighborhood reside in nearby locations in the 1D sequence, which allows their features to interact more easily via convolution operations. Within each window, it is possible to follow x- or y-order to traverse the voxels and collect the non-empty ones into the 1D sequence. Figure 3 shows an example of using the x-order. In our experiments, we observe minimal performance difference between using x-order and y-order.

Note that our serialization operation is only performed once after voxelization. Then, the order of the 1D sequence of voxel tokens remains the same throughout the 3D backbone. This requires minimal data movement to arrange the voxels into a 1D sequence.

3.3. Implicit Voxel Grouping

Given that the number of non-empty voxels is usually in the order of thousands, the dense 1D sequence has a severely imbalanced shape, *e.g.*, $1 \times 6000 \times 128$, where 1 is the batch size, 6000 is the number of non-empty voxels, and 128 is the feature embedding dimension. We observe that this is less efficient on a compact embedded device, as compared to the case where the dimension sizes are more balanced. We speculate that when the dimensions are more balanced, potential underlying parallelization may be utilized to enable faster inference. To make this more concrete, we profile one layer of ConvDotMix on the Qualcomm Hexagon NPU with different input tensor shapes, the result of which is shown in Table 1. Indeed, we can see that when the sizes are more balanced across the batch and token dimensions, the inference is faster.

Motivated by this observation, we propose to reshape

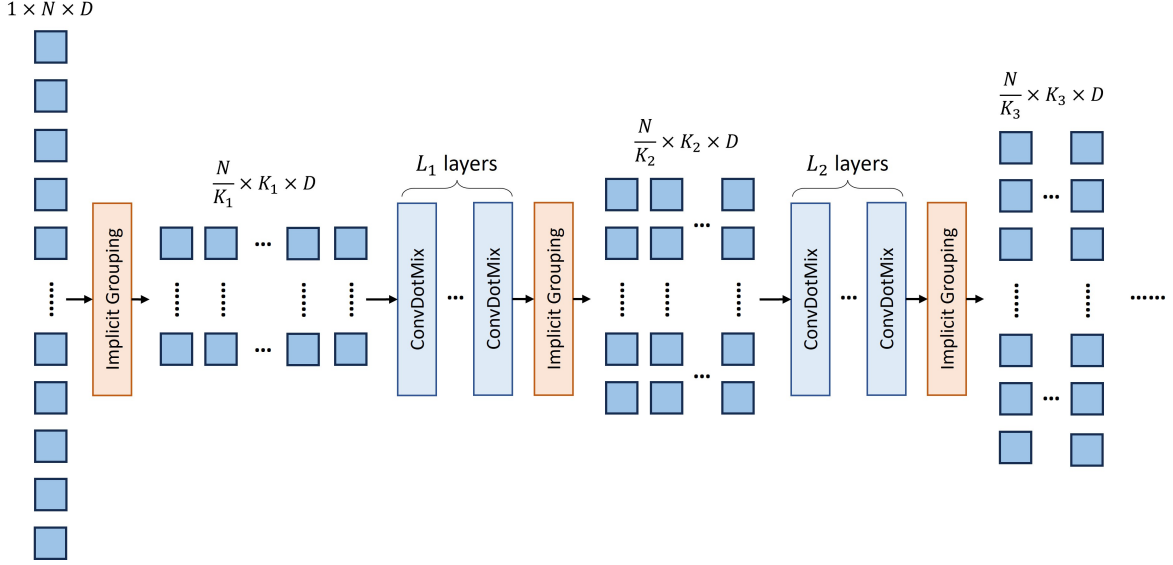


Figure 4. Implicit voxel grouping. The 1D sequence of non-empty voxel tokens with shape $1 \times N \times D$ is converted to $N/K_1 \times K_1 \times D$, which implicitly creates N/K_1 groups of K_1 tokens each. As we proceed to deeper ConvDotMix layers, we use bigger group sizes, e.g., K_2, K_3 , where $K_1 < K_2 < K_3$. Smaller group sizes at the beginning facilitate faster inference and more focused local learning, while larger group sizes at deeper layers work better with the larger effective receptive field.

the 1D sequence and better balance the batch and token dimensions, which implicitly groups the voxels. For instance, when changing the shape from $1 \times 6000 \times 128$ to $10 \times 600 \times 128$, the 6000 voxels are divided into 10 groups of 600 voxels each. While this improves inference speed, such grouping limits the interaction among the voxels, especially when the group size is small. In order to address this, we further propose to use variable, increasing group sizes as we go to deeper ConvDotMix layers. This is because ConvDotMix uses convolutions to perform spatial mixing and with more ConvDotMix layers, the effective receptive field becomes larger and creates wider interaction among the voxels. By increasing the group size in deeper layers, we mitigate its impact on the growing receptive field.

Figure 4 provides an illustration. In earlier layers, we use smaller group sizes, which provide more balanced sizes across the batch and token dimensions for more efficient inference. In deeper layers, we use larger group sizes to account for larger effective receptive fields. Another benefit of using increasing group sizes is that this encourages the network to first aggregate local information, before incorporating bigger spatial contexts in deeper layers. As we shall see in our experiments, increasing group sizes leads to the best performance while a decreasing order is detrimental.

3.4. ConvDotMix

Our devised 3D backbone contains multiple ConvDotMix layers (in addition to the implicit voxel grouping operations). Each ConvDotMix layer is made of large-kernel convolutions operating on the tokens (*i.e.*, non-empty vox-

els), linear layers operating on the embedding dimension, as well as Hadamard product that creates higher-order non-linear interaction among the voxels. More specifically, as shown in Figure 2, the sequence of non-empty voxels (after grouping) goes through linear layers and larger-kernel convolutions. At the same time, a copy of the voxels are mixed channel-wise but without spatial mixing. These two differently mixed versions of voxels are combined via Hadamard product (*i.e.*, element-wise multiplication). In this way, the tokens can interact with each other beyond linear operations. As the effective receptive field becomes larger after several convolution layers, such nonlinear interactions can happen even between two spatially distant voxels. As inspired by MetaFormer [48], we further process the combined features through additional linear layers, as well as add skip connections from the input.

It can be easily seen that all the operations used in ConvDotMix incur only linear computation and memory costs w.r.t. the number of input tokens. Specifically, our use of Hadamard product is inspired by latest works on efficient alternative self-attention schemes [18, 20], which show that such operations can effectively replace the standard self-attention while only incurring linear complexities. Moreover, these ConvDotMix operations, *i.e.*, convolution, MLP, and element-wise multiplication, ultimately boil down to matrix multiplications under the hood, which are well supported on modern compute platforms for AI workloads and can be accelerated by parallelization if it is available on the platform.

Repr.	Method	Key Operators	NDS	mAP	Car	Truck	Bus	T.L.	C.V.	Ped.	M.T.	Bike	T.C.	B.R.
Voxel	CenterPoint [47]	SpConv	64.8	56.4	-	-	-	-	-	-	-	-	-	-
	VoxelNeXt [6]	SpConv	66.7	60.5	83.9	55.5	70.5	38.1	21.1	84.6	62.8	50.0	69.4	69.4
	VISTA [10]	SpConv	68.1	60.8	84.8	57.2	20.5	67.6	36.8	69.0	67.7	50.7	84.1	69.7
	Uni3DETR [41]	SpConv	68.5	61.7	-	-	-	-	-	-	-	-	-	-
	TransFusion-L [1]	SpConv	70.1	65.5	86.9	60.8	73.1	43.4	25.2	87.5	72.9	57.3	77.2	70.3
	LargeKernel3D [5]	SpConv	69.1	63.9	85.1	60.1	72.6	41.4	24.3	85.6	70.8	59.2	72.3	67.7
	LinK [26]	SpConv	69.5	63.6	-	-	-	-	-	-	-	-	-	-
	FSDv2 [13]	SpConv	70.4	64.7	84.4	57.3	75.9	44.1	28.5	86.9	69.5	57.4	72.9	73.6
	SAFDNet[49]	SpConv	71.0	66.3	87.6	60.8	78.0	43.5	26.6	87.8	75.5	58.0	75.0	69.7
Pillar	CenterPoint-Pillars [47]	SpConv	60.2	50.3	-	-	-	-	-	-	-	-	-	-
	PillarNet-18 [33]	SpConv	67.4	59.9	-	-	-	-	-	-	-	-	-	-
	PillarNet-34 [33]	SpConv	67.6	60.2	-	-	-	-	-	-	-	-	-	-
	FastPillars-m [54]	Conv, Attention	68.2	61.7	-	-	-	-	-	-	-	-	-	-
	PillarNeXt-B [21]	SpConv	68.8	62.5	-	-	-	-	-	-	-	-	-	-
	PillarNeSt-Base [27]	Conv, MLP	69.2	63.2	-	-	-	-	-	-	-	-	-	-
	DSVT [40]	Transformer	71.1	66.4	87.4	62.6	75.9	42.1	25.3	88.2	74.8	58.7	77.9	71.0
	FALO (Ours)	Conv, MLP, HP	70.8	65.7	87.1	62.3	75.3	43.0	25.5	87.6	71.9	57.9	77.5	68.7

Table 2. Performance comparison on nuScenes validation set. HP stands for Hadamard product. T.L., C.V., Ped., M.T., T.C., and B.R. stand for trailer, construction vehicle, pedestrian, motorcycle, traffic cone, and barrier, respectively.

Repr.	Method	Key Operators	NDS	mAP	Car	Truck	Bus	T.L.	C.V.	Ped.	M.T.	Bike	T.C.	B.R.
Voxel	CenterPoint [47]	SpConv	65.5	58.0	84.6	51.0	60.2	53.2	17.5	83.4	53.7	28.7	76.7	70.9
	VoxelNeXt [6]	SpConv	70.0	64.5	84.6	53.0	64.7	55.8	28.7	85.8	73.2	45.7	79.0	74.6
	TransFusion-L [1]	SpConv	70.2	65.5	86.2	56.7	66.3	58.8	28.2	86.1	68.3	44.2	82.0	78.2
	LargeKernel3D [5]	SpConv	70.5	65.3	85.9	55.3	66.2	60.2	26.8	85.6	72.5	46.6	80.0	74.3
	LinK [26]	SpConv	71.0	66.3	86.1	55.7	65.7	62.1	30.9	85.8	73.5	47.5	80.4	75.5
	FSDv2 [13]	SpConv	71.7	66.2	83.7	51.6	66.4	59.1	32.5	87.1	71.4	51.7	80.3	78.7
	SAFDNet[49]	SpConv	72.3	68.3	87.3	57.3	68.0	63.7	37.3	89.0	71.1	44.8	84.9	79.5
	PointPillars [19]	MLP	45.3	30.5	68.4	23.0	28.2	23.4	4.1	59.7	27.4	1.1	30.8	38.9
Pillar	PillarNeSt-Base [27]	Conv, MLP	71.3	65.6	87.1	55.5	61.6	62.1	31.0	86.3	69.4	46.8	80.6	76.0
	DSVT [40]	Transformer	72.7	68.4	86.8	58.4	67.3	63.1	37.1	88.0	73.0	47.2	84.9	78.4
	FALO (Ours)	Conv, MLP, HP	70.9	66.1	85.8	56.3	66.7	60.8	33.2	87.0	69.3	44.7	84.1	73.0

Table 3. Performance comparison on nuScenes test set. All reported results are without applying test-time augmentation or model ensemble. HP stands for Hadamard product. T.L., C.V., Ped., M.T., T.C., and B.R. stand for trailer, construction vehicle, pedestrian, motorcycle, traffic cone, and barrier, respectively.

4. Experiments

We perform extensive evaluation of both the efficiency and accuracy of our proposed FALO approach. More specifically, we measure the latency of our model and compare with the latest SOTA on both mobile Orin GPU and Hexagon NPU. We evaluate the detection accuracy on standard benchmarks for LiDAR 3D detection. Further, we conduct extensive ablation study to analyze our proposed designs.

4.1. Datasets and Evaluation Protocol

nuScenes dataset [2] is a widely recognized and challenging benchmark for outdoor 3D perception, offering a perception range of up to 50 meters. It provides comprehensive annotations for various tasks, including 3D object detection and BEV map segmentation. Each frame is annotated at a frequency of 2Hz. The dataset comprises 1,000 scenes, divided into 750 scenes for training, 150 scenes for validation, and 150 scenes for testing, resulting in a total of 40,157 annotated samples. Each sample includes data from six cameras and a 32-beam LiDAR scan.

For 3D object detection, the dataset employs mean Av-

erage Precision (mAP) and the nuScenes Detection Score (NDS) as evaluation metrics. Note that when evaluating model performance, we do not use test-time augmentation or ensemble techniques. These techniques are not practical for real-world applications as they significantly increase the inference cost, *e.g.*, the commonly used double-flip augmentation requires 4 inferences per input sample and quadruples the latency.

Waymo Open Dataset (WOD) [37] is a prominent and well-known benchmark for large-scale outdoor 3D perception. It consists of 1,150 point cloud sequences, totaling over 200,000 frames. Each frame spans a substantial perception range of 150m×150m. The dataset is divided into 798 scenes for training, 202 scenes for validation, and 150 scenes for testing, with each scene containing approximately 200 frames.

For evaluation, WOD employs 3D mean Average Precision (mAP) and mean Average Precision weighted by Heading accuracy (mAPH). These metrics are further divided into two difficulty levels: L1 for objects detected with more than five points and L2 for those detected with at least one point. Similarly, we do not use any test-time augmentation or model ensemble here.

Method	Operator	Vehicle 3D AP/APH		Pedestrian 3D AP/APH		Cyclist 3D AP/APH		mAP/mAPH	mAP/mAPH
		L1	L2	L1	L2	L1	L2	L1	L2
SECOND [42]	SpConv	72.3/71.7	63.9/63.3	68.7/58.2	60.7/51.3	60.6/59.3	58.3/57.0	67.2/63.1	61.0/57.2
PointPillar [19]	SpConv	72.1/71.5	63.6/63.1	70.6/56.7	62.8/50.3	64.4/62.3	61.9/59.9	69.0/63.5	62.8/57.8
CenterPoint [47]	SpConv	74.2/73.6	66.2/65.7	76.6/70.5	68.8/63.2	72.3/71.1	69.7/68.5	74.4/71.7	68.2/65.8
PillarNet-34 [33]	SpConv	79.1/78.6	70.9/70.5	80.6/74.0	72.3/66.2	72.3/71.2	69.7/68.7	77.3/74.6	71.0/68.5
PillarNeXt [21]	SpConv	78.4/77.9	70.3/69.8	82.5/77.1	74.9/69.8	73.2/72.2	70.6/69.6	78.0/75.7	71.9/69.7
VoxelNext [6]	SpConv	78.2/77.7	69.9/69.4	81.5/76.3	73.5/68.6	76.1/74.9	73.3/72.2	78.6/76.3	72.2/70.1
Transfusion [1]	SpConv	-/-	-/65.1	-/-	-/63.7	-/-	-/65.9	-/-	-/64.9
FocalFormer3D [7]	SpConv	-/-	68.1/67.6	-/-	72.7/66.8	-/-	73.7/72.6	-/-	71.5/69.0
HEDNet [51]	SpConv	81.1/80.6	73.2/72.7	84.4/80.0	76.8/72.6	78.7/77.7	75.8/74.9	81.4/79.4	75.3/73.4
SST-TS [12]	Transformer	76.2/75.8	68.0/67.6	81.4/74.0	72.8/65.9	-/-	-/-	-/-	-/-
SWFormer [38]	Transformer	77.8/77.3	69.2/68.8	80.9/72.7	72.5/64.9	-/-	-/-	-/-	-/-
OcTr [53]	Transformer	78.1/77.6	69.8/69.3	80.8/74.4	72.5/66.5	72.6/71.5	69.9/68.9	77.2/74.5	70.7/68.2
DSVT-Pillar [40]	Transformer	79.3/78.8	70.9/70.5	82.8/77.0	75.2/69.8	76.4/75.4	73.6/72.7	79.5/77.1	73.2/71.0
FlatFormer [24]	Transformer	-/-	69.0/68.6	-/-	71.5/65.3	-/-	68.6/67.5	-/-	-/67.2
FastPillars [54]	Conv	-/-	71.5/71.1	-/-	73.2/67.2	-/-	70.5/69.5	-/-	-/69.3
FALO (Ours)	Conv, MLP, HP	78.7/78.3	70.3/69.6	82.6/76.9	75.0/69.6	75.4/74.4	75.4/72.5	78.9/76.5	73.6/70.6

Table 4. Performance comparison on the Waymo Open Dataset validation set. HP stands for Hadamard product.

4.2. Implementation Details

We use 8 ConvDotMix layers in our 3D backbone, with a kernel size 11 for the 1D convolutions and group sizes of 128, 128, 256, 256, 512, 512, 1024, and 1024. No reshaping is needed between layers that use the same group size. We use y-order to serialize the voxels, and there is minimal accuracy difference between using x-order and y-order. Due to the different LiDAR sensors, point cloud densities, and evaluation ranges, we use a pillar size of (0.3m, 0.3m, 8m) for nuScenes data and (0.32m, 0.32m, 6m) for Waymo data, following standard practice. Similar to DSVT [40], we use ResNet layers [17] for the BEV backbone. In the DSVT setup, there are 3 stages of ResNet with 2, 3, and 3 layers each. We create 2 more variants using 3-4-4 and 4-5-5 configurations, respectively. For the detection head, we use the TransFusion [1] head for nuScenes and the CenterPoint [47] head for Waymo.

We choose Nvidia Jetson Orin GPU and Qualcomm Hexagon NPU as the embedded compute platforms to measure model latency. For running a model on device, we first export it to ONNX format. We further use TensorRT when running the model on the Orin GPU. For comparison, we also measure the inference speed of DSVT [40], which is the only available model with SOTA detection accuracy and does not require sparse convolutions.² We also compare with a modified version of PillarNet [33], which is a representative recent pillar-based model. To enable on-device inference, we replace its sparse convolutions with dense ones and have verified that the modified version achieves similar detection accuracy as the original model via retraining.

²While FastPillars [54] and PillarNeSt [27] also claim SOTA performance without using sparse convolutions, they have not made their models publicly available.

4.3. Detection Performance Evaluation

nuScenes. Table 2 and Table 3 summarize the detection performance on nuScenes validation and test sets, respectively. We see that FALO achieves similar detection performance compared to the latest SOTA, *e.g.*, DSVT [40], SAFDNet [49], despite not using expensive, deployment-unfriendly operations like self-attention and 3D sparse convolution. It is noteworthy that without using the 3D voxel representation and 3D sparse convolution, FALO outperforms most voxel-based methods, and additionally, FALO provides significantly better detection accuracy as compared to most pillar-based methods. While PillarNeSt-Base [27] has slightly better accuracy than FALO, it uses the heavy ConvNeXt-Base [23] as the BEV backbone.

Waymo. As summarized in Table 4, our proposed FALO also delivers competitive performance on the Waymo dataset. It achieves detection accuracy on par with SOTA, achieving comparable Average Precision (AP) and Average Precision with Heading (APH) scores across key classes, including vehicles, pedestrians, and cyclists. This result reinforces the generalization and robustness of our proposed efficient FALO architecture across different datasets.

4.4. Latency Evaluation

Figure 1 shows the latency comparison between our proposed FALO models with DSVT [40] and PillarNet [33]. It can be seen that with similar detection performance, FALO achieves significantly higher inference speeds that are $1.6 \times \sim 9.8 \times$ faster than DSVT on Nvidia Jetson Orin GPU and Qualcomm Hexagon NPU. Specifically, FALO offers 24~60 inferences per second on device, enabling real-time, accurate 3D LiDAR object detection operations on mobile autonomous systems, such as self-driving cars and mobile robots. Although PillarNet can also provide ~ 30 inferences per second, its detection accuracy is considerably lower due to the less capable network architecture.

4.5. Ablation Study

In this part, we analyze the effects of various designs in our proposed approach.

Ordering. When serializing the voxels, our proposed ordering is based on local window partitions and traversing voxels in the same neighborhood first before proceeding to the next window. Here, we compare with an variant where no explicit ordering is used, *i.e.*, the voxels are traversed based on their pre-existing order which depends on when the corresponding point is measured by the LiDAR sensor. Table 5 shows that our proposed ordering is effective and improves the detection performance.

Ordering Method	NDS	mAP
No Ordering	69.1	63.0
FALO Ordering	70.2	64.9

Table 5. Effect of our proposed ordering for serializing the voxels into 1D sequence. We use 2-3-3 BEV backbone configuration in this experiment.

Grouping and Group Sizes. The implicit grouping provides two benefits: 1) improving inference speed and 2) encouraging a local-to-global learning. It can be seen in Table 6 that by using our proposed implicit grouping with increasing group sizes, we improve both the accuracy and latency as compared to the baseline that has no grouping. Grouping with constant group sizes provides a very slight detection accuracy improvement. On the other hand, using decreasing group sizes is detrimental to detection performance as it conflicts with the growing effective receptive field as the inference goes deeper through the network.

Grouping Option	NDS	mAP
No Grouping	69.8	64.9
Constant	69.9	64.9
Decreasing	69.7	64.9
Increasing	70.2	64.9

Table 6. Comparison of different grouping options. We use 2-3-3 BEV backbone configuration in this experiment.

ConvDotMix. Our proposed ConvDotMix serves as the core of FALO and provides an efficient, alternative way to process the features as compared to self-attention or 2D/3D sparse convolution. In order to better understand its effectiveness, we use DSVT [40] as the baseline and replace the transformer layers with our ConvDotMix layers. This is the only modification on DSVT in this experiment and we keep the other operations the same as the original DSVT, *e.g.*, window shifting, alternating the voxel serialization between x-order and y-order, etc.

Table 7 shows the result. By replacing the transformer operations with our proposed ConvDotMix, we can even slightly outperform the original DSVT. Moreover, this also reduces the computational cost (in terms of FLOPs) by more than 28% in the 3D backbone. Note that ConvDotMix will

Baseline	Key Operation	NDS	mAP	FLOPs (G)
DSVT [40]	Transformer	71.1	66.4	14.9
	ConvDotMix	71.2	66.6	10.7

Table 7. Comparison of transformer and our proposed ConvDotMix for processing voxels. We use DSVT [40] and compare the performance of these two operations.

be even more efficient when the input 3D point cloud is large and/or the resolution is large, as its complexity scales linearly w.r.t. the number of input tokens, whereas self-attention scales quadratically.

Depth of BEV Backbone. We use 3 ResNet configurations in the BEV backbone, which are 2-3-3, 3-3-4, and 4-5-5; the ResNet contains 3 stages with different number of layers in each stage. As shown in Table 8, using more layers improves the detection performance at the cost of higher latency.

ResNet Config.	NDS	mAP	Latency (ms)	
			Hexagon NPU	Orin GPU
2-3-3	70.2	64.9	33.8	16.6
3-4-4	70.6	65.8	37.8	18.4
4-5-5	70.8	65.7	41.7	21.2

Table 8. Effect of using different numbers of ResNet layers in BEV backbone.

Large Kernel Size. By reducing kernel size from 11 to 5, NDS reduces from 70.8 to 70.2 on nuScenes val. This shows a larger kernel is useful.

5. Conclusions

In this paper, we propose FALO, an efficient and systematic approach for fast and accurate LiDAR-based 3D object detection on resource-constrained computation platforms. Specifically, we proposed ConvDotMix to process the voxels, which consists of large-kernel convolutions, linear layers, and Hadamard products. These operations are computationally efficient and can provide sufficient spatial, channel-wise, and higher-order nonlinear information mixing capabilities to enhance the features. In addition, we proposed other efficient designs to enhance inference speed on hardware, such as a one-time voxel serialization and implicit voxel grouping. Most importantly, when compared to SOTA methods, we eliminate the use of operations that are expensive or infeasible to run on embedded devices, such as sparse convolution, self-attention, window shifting, and voxel re-ordering. FALO achieves real-time inference speeds on modern embedded compute platforms, including the Nvidia Jetson Orin GPU and Qualcomm Hexagon NPU, providing up to $9.8\times$ faster speed compared to latest SOTA. Extensive experiments on standard LiDAR 3D detection benchmarks, such as nuScenes and Waymo, further validate the detection performance of FALO.

References

- [1] Xuyang Bai, Zeyu Hu, Xinge Zhu, Qingqiu Huang, Yilun Chen, Hongbo Fu, and Chiew-Lan Tai. Transfusion: Robust lidar-camera fusion for 3d object detection with transformers. In *Proceedings of the IEEE/CVF conference on computer vision and pattern recognition*, pages 1090–1099, 2022. [6](#), [7](#)
- [2] Holger Caesar, Varun Bankiti, Alex H Lang, Sourabh Vora, Venice Erin Liong, Qiang Xu, Anush Krishnan, Yu Pan, Giancarlo Baldan, and Oscar Beijbom. nuscenes: A multi-modal dataset for autonomous driving. In *Proceedings of the IEEE/CVF conference on computer vision and pattern recognition*, pages 11621–11631, 2020. [6](#)
- [3] Chen Chen, Zhe Chen, Jing Zhang, and Dacheng Tao. Sasa: Semantics-augmented set abstraction for point-based 3d object detection. In *Proceedings of the AAAI Conference on Artificial Intelligence*, pages 221–229, 2022. [3](#)
- [4] Yilun Chen, Shu Liu, Xiaoyong Shen, and Jiaya Jia. Fast point r-cnn. In *Proceedings of the IEEE/CVF international conference on computer vision*, pages 9775–9784, 2019. [3](#)
- [5] Yukang Chen, Jianhui Liu, Xiangyu Zhang, Xiaojuan Qi, and Jiaya Jia. Largekernel3d: Scaling up kernels in 3d sparse cnns. In *Proceedings of the IEEE/CVF Conference on Computer Vision and Pattern Recognition*, pages 13488–13498, 2023. [6](#)
- [6] Yukang Chen, Jianhui Liu, Xiangyu Zhang, Xiaojuan Qi, and Jiaya Jia. Voxelnext: Fully sparse voxelnet for 3d object detection and tracking. In *Proceedings of the IEEE/CVF Conference on Computer Vision and Pattern Recognition*, pages 21674–21683, 2023. [3](#), [6](#), [7](#)
- [7] Yilun Chen, Zhiding Yu, Yukang Chen, Shiyi Lan, Anima Anandkumar, Jiaya Jia, and Jose M Alvarez. Focalformer3d: focusing on hard instance for 3d object detection. In *Proceedings of the IEEE/CVF International Conference on Computer Vision*, pages 8394–8405, 2023. [7](#)
- [8] Bowen Cheng, Lu Sheng, Shaoshuai Shi, Ming Yang, and Dong Xu. Back-tracing representative points for voting-based 3d object detection in point clouds. In *Proceedings of the IEEE/CVF conference on computer vision and pattern recognition*, pages 8963–8972, 2021. [3](#)
- [9] Jiajun Deng, Shaoshuai Shi, Peiwei Li, Wengang Zhou, Yanyong Zhang, and Houqiang Li. Voxel r-cnn: Towards high performance voxel-based 3d object detection. In *Proceedings of the AAAI conference on artificial intelligence*, pages 1201–1209, 2021. [2](#), [3](#)
- [10] Shengheng Deng, Zhihao Liang, Lin Sun, and Kui Jia. Vista: Boosting 3d object detection via dual cross-view spatial attention. In *Proceedings of the IEEE/CVF conference on computer vision and pattern recognition*, pages 8448–8457, 2022. [6](#)
- [11] Shaocong Dong, Lihe Ding, Haiyang Wang, Tingfa Xu, Xinli Xu, Jie Wang, Ziyang Bian, Ying Wang, and Jianan Li. Mssvt: Mixed-scale sparse voxel transformer for 3d object detection on point clouds. *Advances in Neural Information Processing Systems*, 35:11615–11628, 2022. [2](#), [3](#)
- [12] Lue Fan, Ziqi Pang, Tianyuan Zhang, Yu-Xiong Wang, Hang Zhao, Feng Wang, Naiyan Wang, and Zhaoxiang Zhang. Embracing single stride 3d object detector with sparse transformer. In *Proceedings of the IEEE/CVF conference on computer vision and pattern recognition*, pages 8458–8468, 2022. [7](#)
- [13] Lue Fan, Feng Wang, Naiyan Wang, and Zhaoxiang Zhang. Fsd v2: Improving fully sparse 3d object detection with virtual voxels. *arXiv preprint arXiv:2308.03755*, 2023. [6](#)
- [14] Albert Gu and Tri Dao. Mamba: Linear-time sequence modeling with selective state spaces. *arXiv preprint arXiv:2312.00752*, 2023. [3](#)
- [15] Tianrui Guan, Jun Wang, Shiyi Lan, Rohan Chandra, Zuxuan Wu, Larry Davis, and Dinesh Manocha. M3detr: Multi-representation, multi-scale, mutual-relation 3d object detection with transformers. In *Proceedings of the IEEE/CVF winter conference on applications of computer vision*, pages 772–782, 2022. [2](#), [3](#)
- [16] Chenhang He, Hui Zeng, Jianqiang Huang, Xian-Sheng Hua, and Lei Zhang. Structure aware single-stage 3d object detection from point cloud. In *Proceedings of the IEEE/CVF conference on computer vision and pattern recognition*, pages 11873–11882, 2020. [3](#)
- [17] Kaiming He, Xiangyu Zhang, Shaoqing Ren, and Jian Sun. Deep residual learning for image recognition. In *Proceedings of the IEEE conference on computer vision and pattern recognition*, pages 770–778, 2016. [7](#)
- [18] Qibin Hou, Cheng-Ze Lu, Ming-Ming Cheng, and Jiashi Feng. Conv2former: A simple transformer-style convnet for visual recognition. *IEEE Transactions on Pattern Analysis and Machine Intelligence*, 2024. [2](#), [5](#)
- [19] Alex H Lang, Sourabh Vora, Holger Caesar, Lubing Zhou, Jiong Yang, and Oscar Beijbom. Pointpillars: Fast encoders for object detection from point clouds. In *Proceedings of the IEEE/CVF conference on computer vision and pattern recognition*, pages 12697–12705, 2019. [2](#), [3](#), [6](#), [7](#)
- [20] Pierre-David Letourneau, Manish Kumar Singh, Hsin-Pai Cheng, Shizhong Han, Yunxiao Shi, Dalton Jones, Matthew Harper Langston, Hong Cai, and Fatih Porikli. Padre: A unifying polynomial attention drop-in replacement for efficient vision transformer. *arXiv preprint arXiv:2407.11306*, 2024. [2](#), [5](#)
- [21] Jinyu Li, Chenxu Luo, and Xiaodong Yang. Pillarnext: Rethinking network designs for 3d object detection in lidar point clouds. In *Proceedings of the IEEE/CVF Conference on Computer Vision and Pattern Recognition*, pages 17567–17576, 2023. [2](#), [3](#), [6](#), [7](#)
- [22] Zhe Liu, Xin Zhao, Tengting Huang, Ruolan Hu, Yu Zhou, and Xiang Bai. Tanet: Robust 3d object detection from point clouds with triple attention. In *Proceedings of the AAAI conference on artificial intelligence*, pages 11677–11684, 2020. [2](#), [3](#)
- [23] Zhuang Liu, Hanzi Mao, Chao-Yuan Wu, Christoph Feichtenhofer, Trevor Darrell, and Saining Xie. A convnet for the 2020s. In *Proceedings of the IEEE/CVF conference on computer vision and pattern recognition*, pages 11976–11986, 2022. [7](#)
- [24] Zhijian Liu, Xinyu Yang, Haotian Tang, Shang Yang, and Song Han. Flatformer: Flattened window attention for

- efficient point cloud transformer. In *Proceedings of the IEEE/CVF Conference on Computer Vision and Pattern Recognition*, pages 1200–1211, 2023. 2, 7
- [25] Zhe Liu, Jinghua Hou, Xinyu Wang, Xiaoqing Ye, Jingdong Wang, Hengshuang Zhao, and Xiang Bai. Lion: Linear group rnn for 3d object detection in point clouds. *arXiv preprint arXiv:2407.18232*, 2024. 2, 3, 4
- [26] Tao Lu, Xiang Ding, Haisong Liu, Gangshan Wu, and Limin Wang. Link: Linear kernel for lidar-based 3d perception. In *Proceedings of the IEEE/CVF Conference on Computer Vision and Pattern Recognition (CVPR)*, pages 1105–1115, 2023. 6
- [27] Weixin Mao, Tiancai Wang, Diankun Zhang, Junjie Yan, and Osamu Yoshie. Pillarnet: Embracing backbone scaling and pretraining for pillar-based 3d object detection. *IEEE Transactions on Intelligent Vehicles*, 2024. 3, 6, 7
- [28] Xuran Pan, Zhuofan Xia, Shiji Song, Li Erran Li, and Gao Huang. 3d object detection with pointformer. In *Proceedings of the IEEE/CVF conference on computer vision and pattern recognition*, pages 7463–7472, 2021. 3
- [29] Charles R Qi, Hao Su, Kaichun Mo, and Leonidas J Guibas. Pointnet: Deep learning on point sets for 3d classification and segmentation. In *Proceedings of the IEEE conference on computer vision and pattern recognition*, pages 652–660, 2017. 3, 4
- [30] Charles Ruizhongtai Qi, Li Yi, Hao Su, and Leonidas J Guibas. Pointnet++: Deep hierarchical feature learning on point sets in a metric space. *Advances in neural information processing systems*, 30, 2017. 3
- [31] Charles R Qi, Wei Liu, Chenxia Wu, Hao Su, and Leonidas J Guibas. Frustum pointnets for 3d object detection from rgb-d data. In *Proceedings of the IEEE conference on computer vision and pattern recognition*, pages 918–927, 2018. 3
- [32] Charles R Qi, Or Litany, Kaiming He, and Leonidas J Guibas. Deep hough voting for 3d object detection in point clouds. In *proceedings of the IEEE/CVF International Conference on Computer Vision*, pages 9277–9286, 2019. 3
- [33] Guangsheng Shi, Ruifeng Li, and Chao Ma. Pillarnet: Real-time and high-performance pillar-based 3d object detection. In *European Conference on Computer Vision*, pages 35–52. Springer, 2022. 1, 2, 3, 6, 7
- [34] Shaoshuai Shi, Chaoxu Guo, Li Jiang, Zhe Wang, Jianping Shi, Xiaogang Wang, and Hongsheng Li. Pv-rcnn: Point-voxel feature set abstraction for 3d object detection. In *Proceedings of the IEEE/CVF conference on computer vision and pattern recognition*, pages 10529–10538, 2020. 3
- [35] Shaoshuai Shi, Zhe Wang, Jianping Shi, Xiaogang Wang, and Hongsheng Li. From points to parts: 3d object detection from point cloud with part-aware and part-aggregation network. *IEEE transactions on pattern analysis and machine intelligence*, 43(8):2647–2664, 2020. 2, 3
- [36] Shaoshuai Shi, Li Jiang, Jiajun Deng, Zhe Wang, Chaoxu Guo, Jianping Shi, Xiaogang Wang, and Hongsheng Li. Pv-rcnn++: Point-voxel feature set abstraction with local vector representation for 3d object detection. *International Journal of Computer Vision*, 131(2):531–551, 2023. 3
- [37] Pei Sun, Henrik Kretschmar, Xerxes Dotiwalla, Aurelien Chouard, Vijaysai Patnaik, Paul Tsui, James Guo, Yin Zhou, Yuning Chai, Benjamin Caine, et al. Scalability in perception for autonomous driving: Waymo open dataset. In *Proceedings of the IEEE/CVF conference on computer vision and pattern recognition*, pages 2446–2454, 2020. 6
- [38] Pei Sun, Mingxing Tan, Weiyue Wang, Chenxi Liu, Fei Xia, Zhaoqi Leng, and Dragomir Anguelov. Swformer: Sparse window transformer for 3d object detection in point clouds. In *European Conference on Computer Vision*, pages 426–442. Springer, 2022. 7
- [39] Haiyang Wang, Lihe Ding, Shaocong Dong, Shaoshuai Shi, Aoxue Li, Jianan Li, Zhenguo Li, and Liwei Wang. Cagroup3d: Class-aware grouping for 3d object detection on point clouds. *Advances in Neural Information Processing Systems*, 35:29975–29988, 2022. 2, 3
- [40] Haiyang Wang, Chen Shi, Shaoshuai Shi, Meng Lei, Sen Wang, Di He, Bernt Schiele, and Liwei Wang. Dsvt: Dynamic sparse voxel transformer with rotated sets. In *Proceedings of the IEEE/CVF Conference on Computer Vision and Pattern Recognition*, pages 13520–13529, 2023. 1, 2, 3, 4, 6, 7, 8
- [41] Zhenyu Wang, Ya-Li Li, Xi Chen, Hengshuang Zhao, and Shengjin Wang. Uni3detr: Unified 3d detection transformer. *Advances in Neural Information Processing Systems*, 36, 2024. 6
- [42] Yan Yan, Yuxing Mao, and Bo Li. Second: Sparsely embedded convolutional detection. *Sensors*, 18(10):3337, 2018. 2, 3, 7
- [43] Honghui Yang, Wenxiao Wang, Minghao Chen, Binbin Lin, Tong He, Hua Chen, Xiaofei He, and Wanli Ouyang. Pvt-ssd: Single-stage 3d object detector with point-voxel transformer. In *Proceedings of the IEEE/CVF Conference on Computer Vision and Pattern Recognition*, pages 13476–13487, 2023. 3
- [44] Jinrong Yang, Lin Song, Songtao Liu, Weixin Mao, Zeming Li, Xiaoping Li, Hongbin Sun, Jian Sun, and Nanning Zheng. Dbq-ssd: Dynamic ball query for efficient 3d object detection. In *International Conference on Learning Representations*, 2023. 3
- [45] Zetong Yang, Yanan Sun, Shu Liu, Xiaoyong Shen, and Jiaya Jia. Std: Sparse-to-dense 3d object detector for point cloud. In *Proceedings of the IEEE/CVF international conference on computer vision*, pages 1951–1960, 2019.
- [46] Zetong Yang, Yanan Sun, Shu Liu, and Jiaya Jia. 3dssd: Point-based 3d single stage object detector. In *Proceedings of the IEEE/CVF conference on computer vision and pattern recognition*, pages 11040–11048, 2020. 3
- [47] Tianwei Yin, Xingyi Zhou, and Philipp Krahenbuhl. Center-based 3d object detection and tracking. In *Proceedings of the IEEE/CVF conference on computer vision and pattern recognition*, pages 11784–11793, 2021. 2, 3, 6, 7
- [48] Weihao Yu, Mi Luo, Pan Zhou, Chenyang Si, Yichen Zhou, Xinchao Wang, Jiashi Feng, and Shuicheng Yan. Metaformer is actually what you need for vision. In *Proceedings of the IEEE/CVF conference on computer vision and pattern recognition*, pages 10819–10829, 2022. 5
- [49] Gang Zhang, Junnan Chen, Guohuan Gao, Jianmin Li, Si Liu, and Xiaolin Hu. Safdnet: A simple and effective network for fully sparse 3d object detection. In *Proceedings of*

- the IEEE/CVF Conference on Computer Vision and Pattern Recognition*, pages 14477–14486, 2024. [2](#), [3](#), [6](#), [7](#)
- [50] Guowen Zhang, Lue Fan, Chenhang He, Zhen Lei, Zhaoxiang Zhang, and Lei Zhang. Voxel mamba: Group-free state space models for point cloud based 3d object detection. *arXiv preprint arXiv:2406.10700*, 2024. [2](#), [3](#), [4](#)
 - [51] Gang Zhang, Chen Junnan, Guohuan Gao, Jianmin Li, and Xiaolin Hu. Hednet: A hierarchical encoder-decoder network for 3d object detection in point clouds. *Advances in Neural Information Processing Systems*, 36, 2024. [3](#), [7](#)
 - [52] Yifan Zhang, Qingyong Hu, Guoquan Xu, Yanxin Ma, Jianwei Wan, and Yulan Guo. Not all points are equal: Learning highly efficient point-based detectors for 3d lidar point clouds. In *Proceedings of the IEEE/CVF conference on computer vision and pattern recognition*, pages 18953–18962, 2022. [3](#)
 - [53] Chao Zhou, Yanan Zhang, Jiaxin Chen, and Di Huang. Octree-based transformer for 3d object detection. In *Proceedings of the IEEE/CVF conference on computer vision and pattern recognition*, pages 5166–5175, 2023. [7](#)
 - [54] Sifan Zhou, Zhi Tian, Xiangxiang Chu, Xinyu Zhang, Bo Zhang, Xiaobo Lu, Chengjian Feng, Zequn Jie, Patrick Yin Chiang, and Lin Ma. Fastpillars: A deployment-friendly pillar-based 3d detector. *arXiv preprint arXiv:2302.02367*, 9, 2023. [2](#), [3](#), [6](#), [7](#)
 - [55] Yin Zhou and Oncel Tuzel. Voxelnet: End-to-end learning for point cloud based 3d object detection. In *Proceedings of the IEEE conference on computer vision and pattern recognition*, pages 4490–4499, 2018. [2](#)